

High Spin Hall Conductivity in Large-Area Type-II Dirac Semimetal PtTe₂

Hongjun Xu, Jinwu Wei, Hengan Zhou, Jiafeng Feng, Teng Xu, Haifeng Du, Congli He, Yuan Huang, Junwei Zhang, Yizhou Liu, Han-Chun Wu, Chenyang Guo, Xiao Wang, Yao Guang, Hongxiang Wei, Yong Peng, Wanjun Jiang, Guoqiang Yu,* and Xiufeng Han

Manipulation of magnetization by electric-current-induced spin-orbit torque (SOT) is of great importance for spintronic applications because of its merits in energy-efficient and high-speed operation. An ideal material for SOT applications should possess high charge-spin conversion efficiency and high electrical conductivity. Recently, transition metal dichalcogenides (TMDs) emerge as intriguing platforms for SOT study because of their controllability in spin-orbit coupling, conductivity, and energy band topology. Although TMDs show great potentials in SOT applications, the present study is restricted to the mechanically exfoliated samples with small sizes and relatively low conductivities. Here, a manufacturable recipe is developed to fabricate large-area thin films of PtTe₂, a type-II Dirac semimetal, to study their capability of generating SOT. Large SOT efficiency together with high conductivity results in a giant spin Hall conductivity of PtTe₂ thin films, which is the largest value among the presently reported TMDs. It is further demonstrated that the SOT from PtTe₂ layer can switch a perpendicularly magnetized CoTb layer efficiently. This work paves the way for employing PtTe₂-like TMDs for wafer-scale spintronic device applications.


Spin-orbit torque (SOT) provides an ultrafast and energy-efficient means to switch magnetization, which is of fundamental and technical importance for spintronic devices.^[1–5] A typical SOT device consists of heavy metal/ferromagnet (HM/FM) bilayer, where the HM (e.g., Pt, W, Ta, etc.) converts charge current into spin current mainly due to the spin Hall effect (SHE) and then exerts a torque on the adjacent FM enabling magnetization manipulation. To improve the energy efficiency of SOT-driven magnetization switching, considerable efforts have been made to enhance the charge-spin conversion efficiency of HM^[6–9] and reduce the shunting current in the FM.^[10,11] Engineering the bilayer structure^[9,12] or replacing HM by novel materials with larger charge-spin conversion efficiency and higher conductivity^[10,13,14] are possible avenues to realize higher SOT efficiency.

Dr. H. J. Xu, Dr. J. W. Wei, Prof. J. F. Feng, Prof. Y. Huang, Dr. Y. Z. Liu, C. Y. Guo, X. Wang, Y. Guang, Prof. H. X. Wei, Prof. G. Q. Yu, Prof. X. F. Han
Beijing National Laboratory for Condensed Matter Physics
Institute of Physics
University of Chinese Academy of Sciences
Chinese Academy of Sciences
Beijing 100190, China
E-mail: guoqiangyu@iphy.ac.cn

Dr. H. J. Xu, Dr. J. W. Wei, Prof. J. F. Feng, Dr. Y. Z. Liu, C. Y. Guo, X. Wang, Y. Guang, Prof. H. X. Wei, Prof. G. Q. Yu, Prof. X. F. Han
Center of Materials Science and Optoelectronics Engineering
University of Chinese Academy of Sciences
Beijing 100049, China

Dr. H. J. Xu, Dr. J. W. Wei, Prof. G. Q. Yu, Prof. X. F. Han
Songshan Lake Materials Laboratory
Dongguan, Guangdong 523808, China

Dr. H. A. Zhou, Dr. T. Xu, Prof. W. J. Jiang
State Key Laboratory of Low-Dimensional Quantum Physics,
and Department of Physics
Tsinghua University
Beijing 100084, China

 The ORCID identification number(s) for the author(s) of this article can be found under <https://doi.org/10.1002/adma.202000513>.

Dr. H. A. Zhou, Dr. T. Xu, Prof. W. J. Jiang
Collaborative Innovation Center of Quantum Matter
Beijing 100084, China

Prof. H. F. Du
High Magnetic Field Laboratory
Chinese Academy of Sciences
350 Shushanhu Road, Hefei, Anhui 230031, China

Dr. C. L. He
Institute of Advanced Materials
Beijing Normal University
Beijing 100875, China

Dr. J. W. Zhang, Prof. Y. Peng
Key Laboratory of Magnetism and Magnetic Materials of the Ministry of Education
School of Physical Science and Technology and Electron Microscopy
Centre of Lanzhou University
Lanzhou University
Lanzhou 730000, China

Prof. H.-C. Wu
School of Physics
Beijing Institute of Technology
Beijing 100081, China

DOI: 10.1002/adma.202000513

Among numerous new materials, transition metal dichalcogenides (TMDs) are appealing because of their tunable conductivity and spin-orbit coupling,^[15,16] non-trivial energy band topology,^[17] long spin-life time,^[18] and interplay between spin and pseudospin.^[19] Implementing TMDs for SOT devices has shown many advantages, such as controllable SOT by designing crystal symmetry^[20] and electric-field tunability.^[21] However, there are two crucial issues that need to be solved. First, the conductivity of most TMD materials is several orders of magnitude lower than that of HMs, resulting in most of current flowing in FM layer and hence less efficient magnetization switching. Second, the TMD-based SOT devices are usually fabricated by physical exfoliation method, which cannot be extended for practical applications. Thus, metallic TMD thin films with high spin Hall conductivity that can be manufactured on a large scale are demanded for spintronic application. This leaves PtTe₂ as a promising material candidate. PtTe₂ exhibits to date the highest room-temperature electrical conductivity ($\approx 3.3 \times 10^6 \text{ S m}^{-1}$) among metallic TMDs.^[22] In addition, PtTe₂ is categorized as a type-II Dirac semimetal,^[23,24] where the topological nontrivial \mathbb{Z}_2 invariant gives rise to topological surface states (TSSs) with spin-momentum locking (like the case of topological insulator^[25,26]). Although the bulk Dirac node of PtTe₂ and its corresponding TSSs are well below the Fermi level ($\approx -1 \text{ eV}$), another non-trivial conical dispersion located between Γ and M points were found slightly below the Fermi level in PtTe₂.^[24] Similar features in PdTe₂, another type-II Dirac semimetal, were identified as additional TSSs intersecting with Fermi level

from angle-resolved photoemission spectroscopy.^[27] It is thus expected that the TSSs in PtTe₂ might manifest themselves at the Fermi level and be accessible in transport experiments (e.g., SOT measurement). Moreover, the helical spin textures at the Fermi level was observed in few-layer PtTe₂ and ascribed to the local Rashba effect.^[28] Motivated by these intriguing properties, the potential of PtTe₂ in SOT device applications calls for further investigation.

In this work, we developed a simple method to synthesize high-quality large-area PtTe₂ thin films which can be used for SOT devices. We found the SOT efficiency of PtTe₂-based devices (0.09–0.15 for 5 nm-thick PtTe₂ layer) is 1.5–2 times larger than that of a 4 nm-thick Pt-based control sample. The spin Hall conductivity of PtTe₂ ($0.2\text{--}2 \times 10^5 \hbar/2e (\Omega \text{ m})^{-1}$) is the largest among the presently studied TMDs and comparable to that of Pt and topological insulator. Taking advantage of the large SOT of PtTe₂, we have further realized efficient switching of perpendicular magnetization in PtTe₂/Au/CoTb devices.

Large-area high-quality PtTe₂ films are obtained through a two-step process, which has been previously used for fabricating PtSe₂ and PtS₂ thin films.^[29–32] Large-area Pt thin films with nominal thicknesses of 0.5–4 nm were first prepared on Si/SiO₂ wafers by a magnetron sputtering system. We then transformed the Pt thin films into uniform and homogenous PtTe₂ thin films by annealing them in tellurium vapor at $\approx 460 \text{ }^\circ\text{C}$ (see Figure 1a,b, details can be found in experimental part). As a CdI₂-type trigonal (1T) crystal, PtTe₂ is composed of edge-shared PtTe₆ octahedra which form the basal *a-b* planes (see Figure S1a

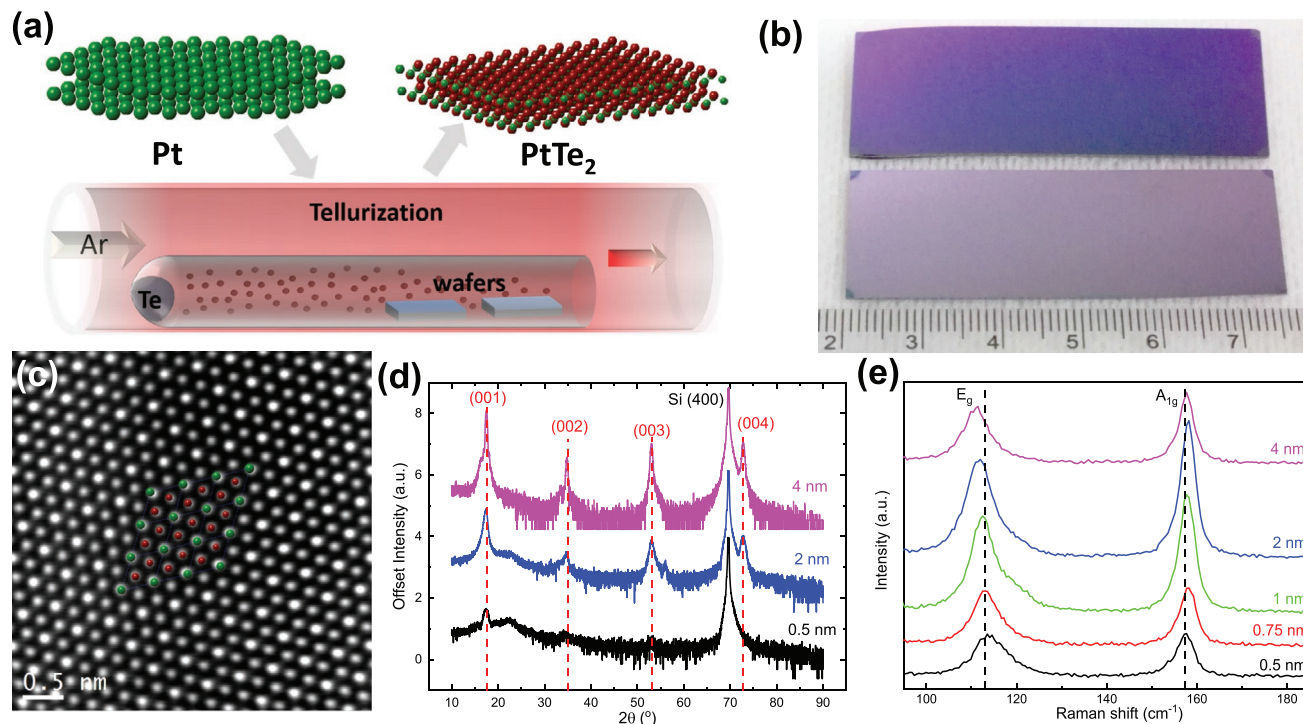


Figure 1. Structure of PtTe₂ thin film. a) Schematic illustration of the CVD process that transforms large-scale Pt thin films into PtTe₂ thin films. b) Large-scale PtTe₂ thin films with thicknesses of $\approx 5 \text{ nm}$ (top) and $\approx 10 \text{ nm}$ (bottom). The rule is in a unit of centimeter. c) HRTEM image of a typical PtTe₂ thin film with thickness $\approx 5 \text{ nm}$. In the middle, the overlaid Pt–Te atomic model shows the matching between ideal PtTe₂ (001) pattern with the real atoms. d) X-ray diffraction and e) Raman spectra for various PtTe₂ thin films (initial Pt thicknesses are labeled). Note that the green and red spheres in (a) and (c) present schematic Pt atoms and Te atoms, respectively.

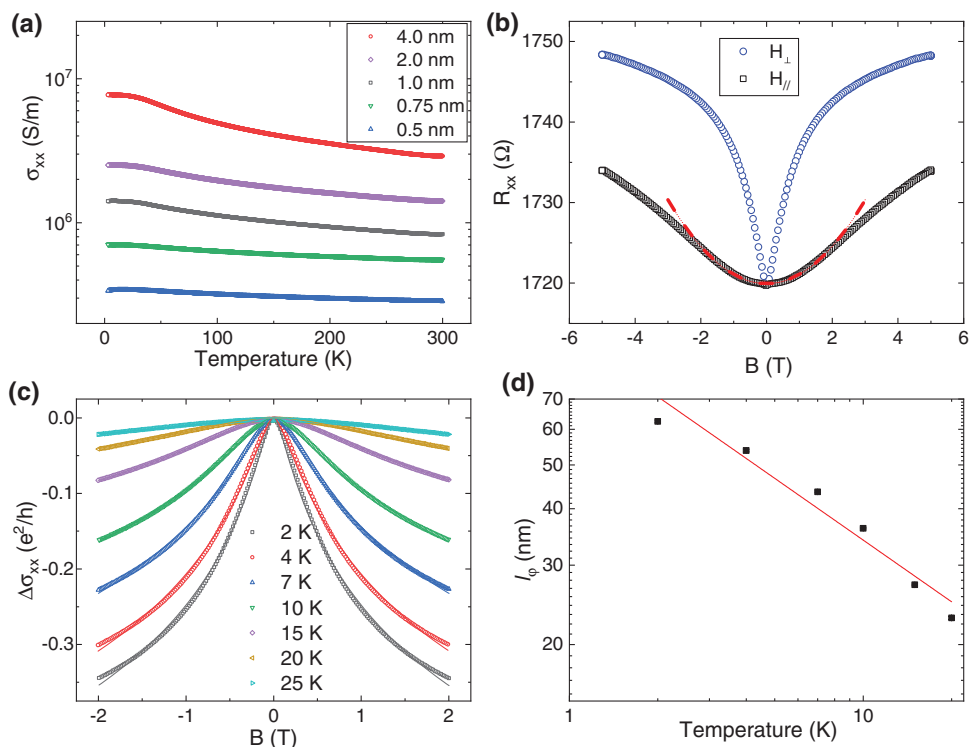


Figure 2. Transport properties of PtTe₂ thin films. a) Temperature dependence of conductivity in PtTe₂ thin films (the numbers are the nominal thicknesses of the initial Pt thin films). b) MR of a PtTe₂ thin film (≈ 3 nm) at 2 K for magnetic field along with two different directions. The dashed line is parabolic fitting of MR under H_{\parallel} . c) Magnetoconductance of the PtTe₂ thin film at low temperature under H_{\perp} , where $\Delta\sigma_{xx} = (L/Wt)/R_{xx}$, L , W , and t are length, width, and thickness of PtTe₂ channel. d) Temperature dependence of phase decoherence length l_{ϕ} and its fitting with $l_{\phi} \propto T^{-\gamma}$.

in the Supporting Information).^[33] A strong interaction in Te layers makes their P_z valence bands more dispersive, which is the origin of the typical metallic behavior in PtTe₂.^[34] The lattice parameters for PtTe₂ are $a = b = 4.03$ Å and $c = 5.22$ Å.^[24] All the PtTe₂ thin films are orientated in the (001) direction as reflected by the (001) series peaks in the X-ray diffraction spectra (indexed in Figure 1d). High-resolution transmission electron microscopy (HRTEM) images indicate that the PtTe₂ thin films are polycrystal with typical grain sizes of up to 20–50 nm (see Figure S1c in the Supporting Information). The hexagonal atomic pattern in the HRTEM image perfectly matches the PtTe₂ (001) structure with $a = b \approx 4.03$ Å, showing the high-quality crystal structure of the PtTe₂ thin films (Figure 1c). The Raman spectra of the studied samples are shown in Figure 1e. Two peaks are identified as the different vibrational modes of PtTe₂ lattice: the peak around 111 cm⁻¹ is the E_g mode resulting from the in-plane Te–Pt–Te lattice vibration and the 158 cm⁻¹ one matches up to the A_{1g} mode due to the out-of-plane vibration. As the thickness increases from ≈ 3 to ≈ 20 nm, the E_g mode shifts from 114 to 111 cm⁻¹ while the change of A_{1g} is not clear. Such a trend is in agreement with the results of PtTe₂ crystals grown by the chemical vapor deposition (CVD) method.^[35] The 0.5–4 nm Pt thin films become 3–20 nm PtTe₂ after transformation, which are measured by atomic force microscopy (AFM). Their root-means-square (RMS) roughnesses are all less than 0.7 nm in a $5 \times 5 \mu\text{m}^2$ area (Figure S1b, Supporting Information). These large, uniform, smooth, and high-quality PtTe₂ thin films are thus suitable for devices application.

The conductivity of the PtTe₂ thin films (3–20 nm) at room temperature is in the range of $0.2\text{--}3 \times 10^6$ S m⁻¹, as shown in Figure 2a, which is consistent with that of single-crystal PtTe₂ flakes.^[35] This again indicates the high quality of these thin films. The increase of conductivity upon decreasing temperature signifies their metallic behavior. Figure 2b,c shows the magnetoresistances (MR) and magnetoconductance of a 3 nm-thick PtTe₂ thin film for magnetic field applied along the current (H_{\parallel}) and perpendicular (H_{\perp}) to the film plane at 2 K. The remarkable difference in MR between H_{\parallel} ($\text{MR} \propto B^2$ when $B < 2$ T) and H_{\perp} is probably related to the confined vertical dimension of thin film or the chiral anomaly of Dirac fermions.^[36] The MR under H_{\perp} obviously deviates from the parabolic behavior at low temperature for all the PtTe₂ thin films, which is the typical signature of weak antilocalization (WAL). WAL is usually considered as an indication of strong spin–orbit coupling.^[15,37] WAL persists up to ≈ 30 K and the magnetoconductance curves can be fitted by the Hikami–Larkin–Nagaoka (HLN) model^[38]

$$\Delta\sigma(B) = \frac{\alpha e^2}{\pi h} \left[\ln\left(\frac{B_{\phi}}{B}\right) - \psi\left(\frac{1}{2} + \frac{B_{\phi}}{B}\right) \right] \quad (1)$$

Here, α is the fitting constant, e is the electron charge, h is the Planck's constant, Ψ is the digamma function, and B_{ϕ} is related to the phase decoherence length $l_{\phi} = \sqrt{\hbar/8\pi e B_{\phi}}$. Fitting the conductance from 2–25 K (Figure 2c), the corresponding l_{ϕ} are extracted to be ≈ 60 nm at 2 K. The l_{ϕ} decreases to ≈ 20 nm when the temperature increases to 20 K, as shown in Figure 2d.

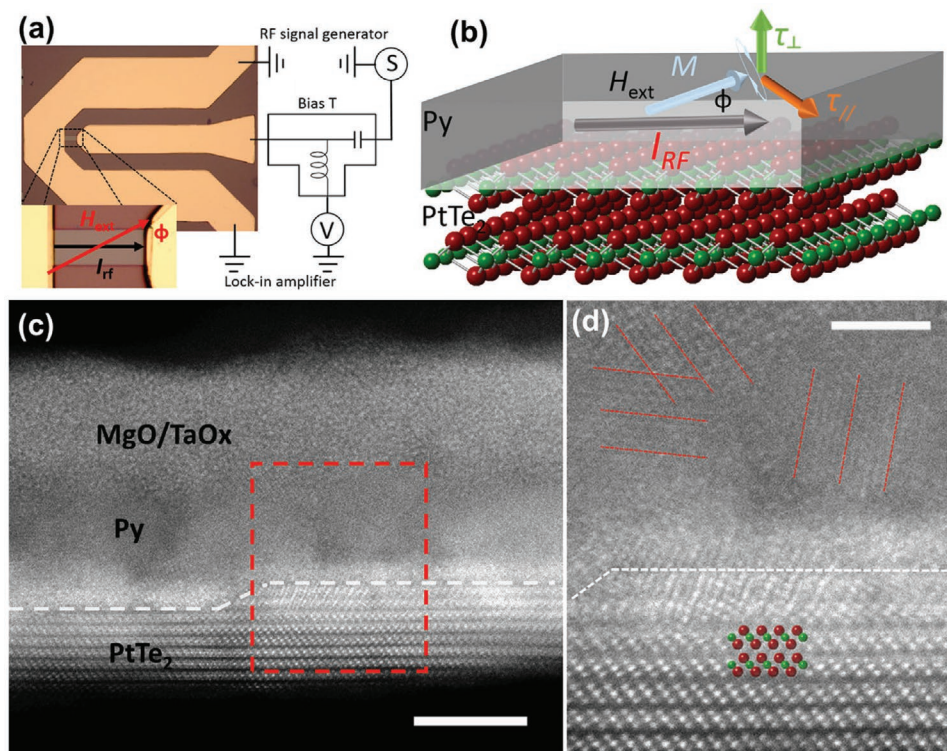


Figure 3. Schematic illustration of PtTe₂/Py bilayer for studying SOT. a) Layout of ST-FMR device with GSG connection. The I_{rf} flows along the longitudinal direction of the rectangular bars (x -axis). The angle between I_{rf} and the external field is ϕ . b) I_{rf} flowing in PtTe₂ generates a SOT including in-plane (τ_{\parallel}) and out-of-plane (τ_{\perp}) components and drives magnetization of Py into precession around the effective field direction. c) Cross-sectional HAADF-STEM image of a PtTe₂/Py stack, where the interface is indicated by the white dashed lines and d) the rectangular region is magnified, where the overlaid atomic model shows the Pt (green) and Te (red) atoms forming high-quality PtTe₂ lattices (with 1T structure) and the parallel red dashed lines mark the lattices of Py. The scale bars are 5 and 2 nm in (c) and (d), respectively.

The temperature dependence of l_{ϕ} can be fitted as $l_{\phi} \propto T^{-\gamma}$ and $\gamma \approx 0.45$ was obtained which implies the electron dephasing in PtTe₂ thin film is dominated by electron-electron interactions ($\gamma = 0.5$) rather than the electron-phonon interaction ($\gamma = 1$). The range of l_{ϕ} and the electron scattering mechanism in our thin-film samples are consistent with the results of single-crystal PtTe₂.^[22]

Next, we fabricate PtTe₂/FM hybrid structures and characterize the current-induced SOT. After preparation of the PtTe₂ films, we immediately transferred them into a sputtering system to minimize the contamination of the surface. Permalloy (Py) layers with various thicknesses were sputtered onto the PtTe₂ thin films followed by the capping layers of MgO(2)/Ta(1.5) (numbers in brackets are in nanometers throughout this paper). Figure 3c,d shows the high-angle annular dark-field scanning transmission electron microscopy (HAADF-STEM) images for the cross-section of the multilayer. A sharp interface is identified where the underneath PtTe₂ owns perfect layered structures with atomic steps. Most of the PtTe₂ at the interface remains intact due to its stability.^[39] It is noted that some regions of the top layer are obscure, which might be related to air exposure during the transfer.

We characterize the SOT using the spin-torque ferromagnetic resonance (ST-FMR) technique.^[40] Ground-Source-Ground (GSG) electrodes were deposited for radio-frequency (RF) signal injection and DC voltage signal detection (as illustrated in Figure 3a).

In the ST-FMR experiments, the oscillatory resistance due to SOT-induced magnetization precession together with RF current leads to a rectified mixing voltage (V_{mix}).^[41] V_{mix} is picked up by a lock-in amplifier and it can be decomposed as: $V_{mix} = V_S F_S + V_A F_A$, where the symmetric Lorentzian component is $F_S(H_{ext}) = \Delta H^2 / [(H_{ext} - H_r)^2 + \Delta H^2]$ and the antisymmetric Lorentzian component is $F_A(H_{ext}) = \Delta H^2 (H_{ext} - H_r) / [(H_{ext} - H_r)^2 + \Delta H^2]$. Here, ΔH is the linewidth of V_{mix} curve, H_{ext} is the external magnetic field, and H_r is the resonant field. V_S and V_A are the amplitudes of the symmetric and antisymmetric components which are proportional to the in-plane damping-like torque and out-of-plane torques, respectively (see Figure 3b).^[41] Typical frequency-dependent ST-FMR spectra and V_{mix} for sample PtTe₂(5)/Py(t) are shown in Figure 4a–c. To exclude possible parasitic effects,^[25] angular dependence of $V_{S(A)}$ is obtained by sweeping in-plane magnetic field along with different directions (ϕ , relative to $+x$ -axis). Normally, $V_{S(A)} \propto V_{S(A)}^0 \sin 2\phi \cos \phi$, where $V_{S(A)}^0$ is the averaged amplitude for V_S (V_A), the $\sin 2\phi$ and $\cos \phi$ parts are derived from angular magnetoresistance and the torque $\propto \mathbf{m} \times \hat{\mathbf{y}}$ respectively. For comparison, the angular dependence of V_S and V_A for the cases of $t = 2.5$ and 10 nm are shown in Figure 4e,f, respectively. Both V_S and V_A are well-fitted by above angular dependence, which excludes the contribution from spin Seebeck effect (in that case, $V_S \propto \sin \phi$)^[42] and the possibility that the spin orientation deviates from γ -axis.^[20] Note that spin-pumping generates symmetric signals with the same angular dependence as

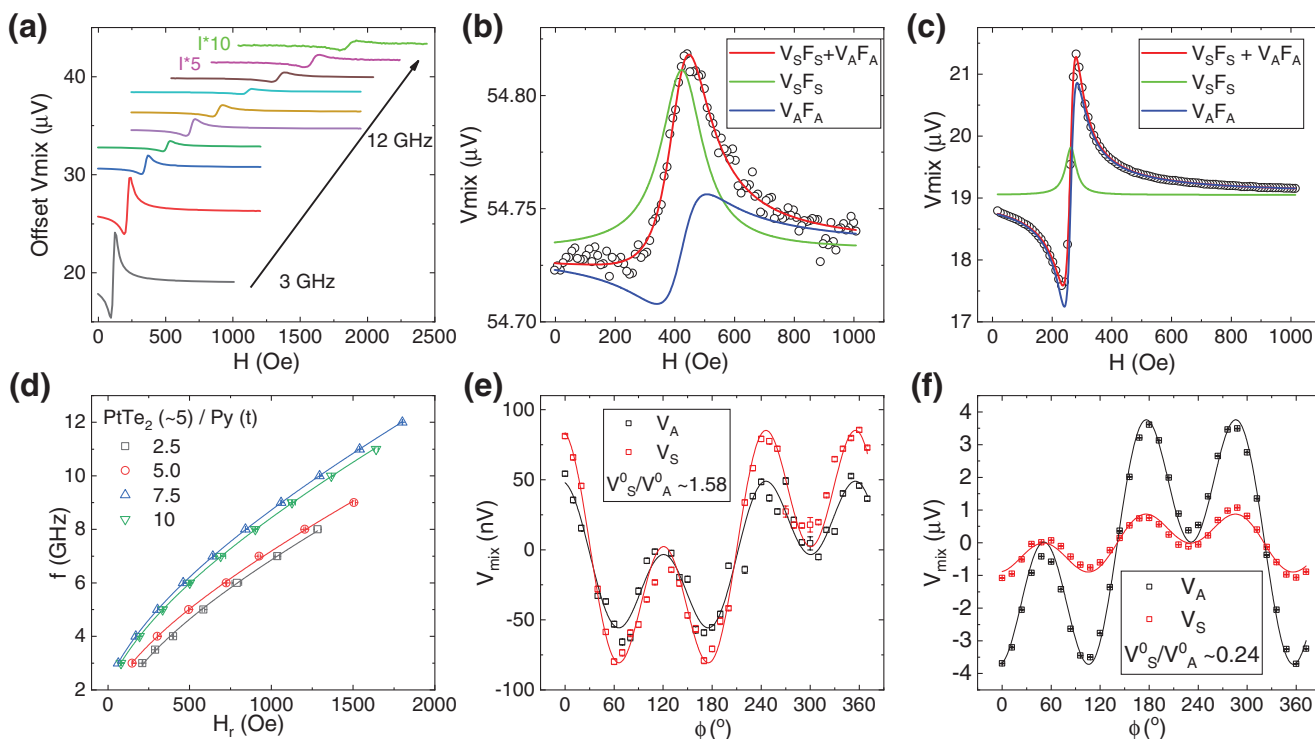


Figure 4. ST-FMR results of PtTe₂/Py stacks. a) Frequency dependence (from 3 to 12 GHz) of V_{mix} for PtTe₂ (5)/Py (10). Typical V_{mix} and the corresponding Lorentzian fitting for b) PtTe₂ (5)/Py (2.5) and c) PtTe₂ (5)/Py (10) are shown. It was measured under 4 GHz RF excitation and $\phi \approx 35^\circ$ where the largest V_{mix} is obtained. d–f) From the Lorentzian fitting, V_S , V_A , and H_r are extracted for plots. d) f versus H_r for different Py thicknesses. From fittings with Kittel's formula, M_{eff} is deduced for each stack. e, f) Angular dependence of V_A and V_S and the corresponding $\sin 2\phi \cos \phi$ fittings for PtTe₂ (5)/Py (2.5) and PtTe₂ (5)/Py (10), respectively.

the V_S from damping-like torque in ST-FMR,^[25] but such contribution is negligible (see supporting material).^[43,44] The SOT efficiency ξ_{SOT} can be expressed as

$$\xi_{\text{SOT}} = (V_S^0/V_A^0) \left(\frac{e\mu_0 M_s t d}{\hbar} \right) \left[1 + (4\pi M_{\text{eff}}/H_{\text{ext}}) \right]^{1/2} \quad (2)$$

Here, \hbar is the reduced Planck's constant, μ_0 is the permeability of free space, M_s is the saturation magnetization, t is the thickness of FM, and d is the thickness of nonmagnetic (NM) layer that generates SOT. M_{eff} is the effective magnetization of FM/NM bilayer, which can be acquired from fitting frequency-dependent resonant field with Kittel's formula (see Figure 4d). ξ_{SOT} is related to the spin Hall angle θ_{SH} by the relation of $\xi_{\text{SOT}} = T\theta_{\text{SH}}$, where T is the interface spin transparency. On the other hand, V_A signifies the out-of-plane torques which include field-like torque and the torque due to Oersted field. To extract the two contributions in V_A , thickness dependence of ξ_{SOT} can be used as^[6]

$$\frac{1}{\xi_{\text{SOT}}} = \frac{1}{\xi_{\text{DL}}} \left(1 + \frac{\hbar}{e \mu_0 M_s d t} \xi_{\text{FL}} \right) \quad (3)$$

Here, $\xi_{\text{DL (FL)}} = \mu_0 M_s d_F H_{\text{DL (FL)}} (2e/\hbar) / jc$ is the SOT efficiency due to damping-like (field-like) torque. To plot $1/\xi_{\text{SOT}}$ as a function of $1/t$, a series of samples, PtTe₂ (≈ 5)/Py (t) with $t = 2.5$ –10 nm, were fabricated at the same batch. The representative results are shown in Figures 4 and 5 (see the other

results from the control samples in Figure S3 in the Supporting Information). The $\xi_{\text{DL (FL)}}$ are obtained to be: $\xi_{\text{DL}} \approx 0.09$ and $\xi_{\text{FL}} \approx -0.004$ by linearly fitting $1/\xi_{\text{SOT}}$ (Figure 5a). These values are comparable to that of Pt reported in the literature.^[40] Control samples of Pt (4)/Py (t) were also prepared in the same batch for comparison. To fairly compare $\xi_{\text{DL (FL)}}$ between PtTe₂ and Pt, the Pt thin films were exposed to air before sputtering Py for the control sample. The results are plotted in Figure 5a as well (V_S^0/V_A^0 are shown in Figure S4 in the Supporting Information). We found $\xi_{\text{DL}} \approx 0.058$ and $\xi_{\text{FL}} \approx -0.002$ for Pt, which are consistent with the previous reports.^[45,46] Hence, PtTe₂ presents a larger SOT efficiency than Pt. The $\xi_{\text{DL (FL)}}$ of PtTe₂ can be further improved by minimizing the air exposure time and reducing the surface roughness as presented by the red circles in Figure 5a with $\xi_{\text{DL}} \approx 0.152$ and $\xi_{\text{FL}} \approx -0.004$ (samples prepared at a different batch). In conjunction with its conductivity (see σ_{xx} in Figure S2c in the Supporting Information), the spin Hall conductivity ($\sigma_{\text{SH}} = \sigma_{xx} \theta_{\text{SH}}$) of PtTe₂ reaches up to 1.6×10^5 ($\hbar/2e$) ($\Omega \text{ m}$)⁻¹. As shown in Table 1, the obtained spin Hall conductivity in the studied PtTe₂ polycrystalline thin films is the largest one among TMDs reported so far. The value is even comparable to the values of Bi₂Se₃, a representative topological insulator. The large spin Hall conductivity is because the SOT efficiency and electrical conductivity of PtTe₂ are both large. This superior property is beneficial for low-dissipation applications.

To further explore the origin of the relatively large SOT in PtTe₂, we also characterized the SOT efficiency in various PtTe₂ (d)/Py (5) samples ($d \approx 3$ –20 nm). As shown in Figure 5b, the

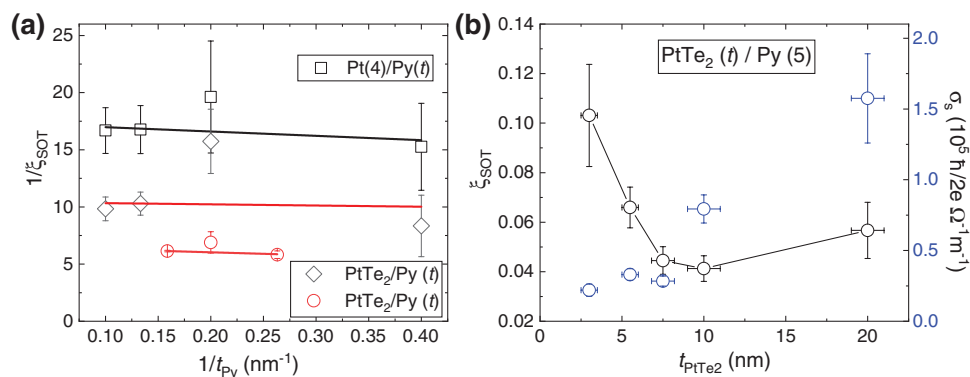


Figure 5. a) $1/\xi_{\text{SOT}}$ versus $1/t_{\text{Py}}$ for PtTe₂/Py (circles) and Pt/Py (squares) and the corresponding linear fitting. Note that there are two series of PtTe₂-based devices (in different colors) prepared at different batches. b) Thickness dependence of ξ_{SOT} and spin Hall conductivity σ_s . Here we assume $T \approx 1$ in $\theta_{\text{SH}} = \xi_{\text{SOT}}/T$, which actually presents the lower limit of θ_{SH} .

ξ_{SOT} first decreases from ≈ 0.1 to 0.04. It then increases and saturates at 0.057 ± 0.011 . This nonmonotonic behavior implies that the SOT (with positive ξ_{SOT}) in PtTe₂ might originate from different sources. In general, an increase with a saturation of ξ_{SOT} on the thickness is expected when the SOT originates from the bulk SHE.^[45] Obviously, the thickness dependence of ξ_{SOT} (when $d < 10$ nm) is different from the expectation, indicating that SHE is not the sole origin of the SOT in the studied samples. The interface between PtTe₂ and Py might play a role through the Rashba–Edelstein effect.^[28] However, in that case, a significant field-like torque^[47] and a negative ξ_{SOT} would appear,^[25] which is in contradiction with our observation. It was reported in Bi_xSe_{1-x} nanocrystalline thin films that the enhanced ξ_{SOT} can be ascribed to the quantum confinement effect from tiny crystal grains (≈ 6 nm).^[14] However, the normal grain sizes of 20–50 nm in our samples are much larger than that “quantum size.” It is thus not reasonable to attribute our results to quantum confinement. On the other hand, the TSSs of PtTe₂ at the Fermi level might manifest themselves (like PdTe₂)^[27] in SOT owing to the spin-momentum locking. The PtTe₂ thickness dependence of ξ_{SOT} in our PtTe₂/Py bilayer is similar to that in Bi₂Se₃/Co₄₀Fe₄₀B₂₀.^[48]

In the Bi₂Se₃/Co₄₀Fe₄₀B₂₀ bilayer, the higher and lower ξ_{SOT} in the thinner and thicker Bi₂Se₃ film were ascribed to the TSSs and SHE, respectively. The SOT comparison between PtTe₂ and Bi₂Se₃ may suggest that the TSSs of PtTe₂ contribute to the SOT in the studied sample. Further study is required to investigate more details about the origin of the large SOT in PtTe₂.

We subsequently implement the studied PtTe₂ thin films for efficiently switching magnetic moments. A robust bulk perpendicularly magnetized CoTb layer^[49] was grown onto PtTe₂ thin films. A thin Au layer (≈ 2.5 nm) was deposited before CoTb to avoid degrading its bottom surface due to the physically adsorbing oxygen and water molecules on the PtTe₂ surface. The patterned Hall-bar devices for measurement are depicted in **Figure 6a**. An in-plane magnetic field along *x*-axis (H_x) is required for a deterministic switching of perpendicular magnetization.^[3] DC current pulses (width ≈ 50 ms) are applied along *x*-axis which induces a SOT on the CoTb layer and switching its magnetic moments. This magnetization orientation is characterized by measuring the signals of anomalous Hall effect (AHE) after each current pulse (delay ≈ 25 ms). The PtTe₂/Au/CoTb stack exhibits a perpendicular magnetic anisotropy

Table 1. A comparison of SOT in PtTe₂ with other TMD materials, topological insulator Bi₂Se₃, and heavy metal Pt.

SOT Materials	Fabrication method	Conductivity [$\Omega \text{ m}$] ⁻¹	Spin Hall angle [θ_{SH}]	Spin Hall conductivity [$(\hbar/2e)(\Omega \text{ m})^{-1}$]	Refs.
TMDs:					
MoS ₂	Exfoliation	1.4×10^3	0.033	47	[53]
WTe ₂ ^{a)}	Exfoliation	2.6×10^5 $1.4\text{--}1.7 \times 10^5$	≈ 0.029 0.09–0.5	$\approx 8 \times 10^3$ $0.4\text{--}6 \times 10^4$	[20] [54]
NbSe ₂	Exfoliation	6×10^5	0.005–0.013	$3\text{--}8 \times 10^3$	[55]
MoTe ₂	Exfoliation	1.8×10^5	0.032	$\approx 5.8 \times 10^3$	[56]
PtTe ₂	Two-step process	$0.3\text{--}3 \times 10^6$	0.05–0.15	$0.2\text{--}1.6 \times 10^5$	This work
Topological insulators and Pt:					
Bi ₂ Se ₃	Molecular beam epitaxy	$\approx 1 \times 10^5$ 5.7×10^4	0.16 2–3.5	1.6×10^4 $1\text{--}2 \times 10^5$	[49] [25]
Bi _x Se _{1-x}	Sputter	7.8×10^3	18.62	1.45×10^5	[14]
Pt	Sputter	$2\text{--}5 \times 10^6$ 5×10^6	0.02–0.1 0.076	3.5×10^5 3.8×10^5	[45] [40]

^{a)}Note that for measuring SOT in WTe₂, the current direction was along *a*-axis of WTe₂ crystal in ref. [20], while it was along the *b*-axis in ref. [54].

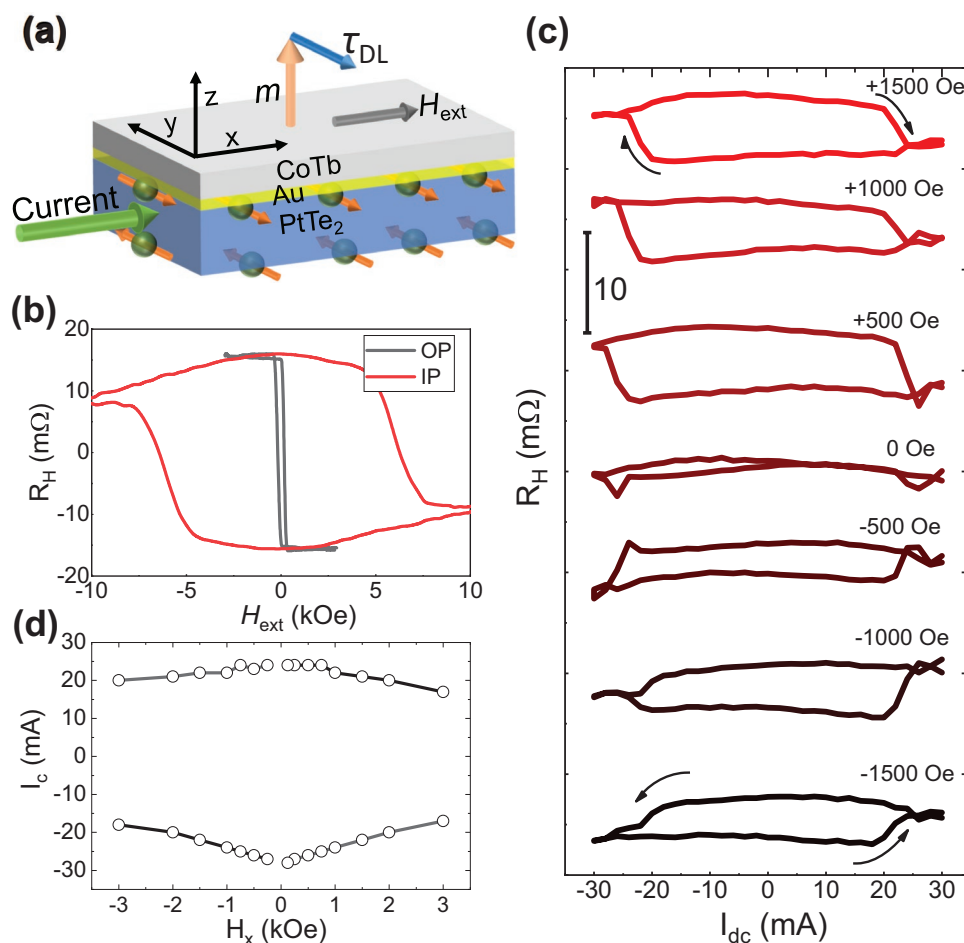


Figure 6. Current-induced switching of the CoTb layer by SOT from PtTe₂. a) Schematic layout for PtTe₂/Au/CoTb stack and the SOT generated by the majority of current flowing in PtTe₂. b) AHE of PtTe₂/Au/CoTb stacks with scanning the external magnetic field along the x axis (red curve) and the z axis, respectively. c) Switching of CoTb by SOT from PtTe₂ under different in-plane field, *H*_x. d) Switching phase diagram for the PtTe₂/Au/CoTb heterostructure, where *I*_c is the critical switching current.

(PMA), as shown in Figure 6b. Switching behavior is observed when the DC current is larger than 20 mA ($j_c \approx 9.9 \times 10^6$ A cm⁻² in PtTe₂ under $H_x \approx 2$ kOe). The switching chirality is reversed after reversing the direction of *H*_x, which is consistent with the SOT switching behavior (Figure 6c). The maximum change of AHE by SOT-induced switching is ≈ 8 mΩ, indicating an uncompleted switching. We speculate that this uncompleted switching is related to broadening of current path (i.e., lower current density locally) at the cross section region of the Hall bar configuration.^[50] With increasing *H*_x, a smaller switching current is required and the corresponding change of AHE becomes smaller (Figure 6c,d), which are typical features of SOT switching.^[51] The control experiment reveals that there is no SOT switching in the Au (2.5)/CoTb(6) sample for DC current density of up to $\approx 1.2 \times 10^7$ A cm⁻², which is already ≈ 4 times larger than the current density in PtTe₂ (10)/Au (2.5)/CoTb (6) ($\approx 3.1 \times 10^6$ A cm⁻²) (see Figure S6 in the Supporting Information). The critical switching current density is in general proportional to the saturation magnetization and anisotropy energy.^[3] From vibrating sample magnetometer and AHE measurements, it is found that Au (2.5)/CoTb (6) bilayer has a weaker PMA thus it should be easier to switch. However, even

larger current density flowing in Au/CoTb cannot trigger the switching. The absence of current-driven switching in the control sample is reasonable because of the relatively small spin Hall angle in Au.^[52] Therefore, the switching behavior in PtTe₂ (10)/Au (2.5)/CoTb (6) must be dominated by the current-induced SOT from PtTe₂. On the other hand, we also prepared Pt (4)/Au(2.5)/CoTb (6) stacks. A higher critical current density in Pt, $j_c \approx 3.7 \times 10^7$ A cm⁻², is required to switch the magnetization of CoTb (Figure S6f, Supporting Information). Considering the thicknesses, the critical current in Pt is roughly 1.5 times larger than that in PtTe₂. It implies that the 10 nm-thick PtTe₂ layer (transformed from 2 nm-thick Pt) is more efficient in charge-to-spin conversion than a 4 nm-thick Pt layer.

In conclusion, we demonstrated that homogenous high-quality PtTe₂ thin films with high conductivity and strong spin-orbit coupling can be synthesized in a manufacturable manner. From ST-FMR measurements, substantial SOT dominated by the damping-like torque was established in the PtTe₂/Py bilayer, where the TSSs of PtTe₂ might play an important role. It suggests that PtTe₂ is a compelling material for low-power SOT devices and other applications related to charge-spin interconversion. In order to be compatible with modern spintronic technology,

transferring the as-grown PtTe₂ sample from CVD furnace into sputter system without air exposure is required, which can further enhance the device performance. This work presents a facile strategy to investigate potential TMD materials for spintronics.

Experimental Section

Sample Preparation and Characterization: PtTe₂ thin films were transformed from Pt thin films by annealing the sources in a CVD furnace. Si/SiO₂ wafers with sputtered Pt films and Te source were loaded into half-open quartz tube as shown in Figure 1a. The system was first evacuated (base pressure ≤ 1 Pa) and then protected by flowing a gas mixture, Ar/H₂ (19:1), with a rate of 100 standard cubic centimeters per minute. The reaction temperature was ≈460 °C and the typical reaction time was 5–10 min with a pressure ≈60 Pa. Py (Ni₈₀Fe₂₀) layers were directly sputtered onto PtTe₂ thin films (power ≈ 120 W) after transferring the samples from CVD furnace into a magnetron sputtering chamber and protected by MgO/Ta. The 6 nm-thick CoTb layer was prepared by co-sputtering of Co and Tb, in which the atomic ratio of Co/Tb was ≈2.9, and capped with SiN_x/Ta. Raman analysis was carried out using a HORIBA Raman microscope with an excitation wavelength of 532 nm. As-grown films were transferring onto TEM grids for STEM.^[31] Cross-section samples of the multilayer devices were fabricated by using a focused ion-beam system. HAADF-STEM studies were performed in JEM-ARM200 spherical aberration-corrected transmission electron microscope.

Device Fabrication and Measurement: Two types of devices were made. For ST-FMR experiments, the stacks of PtTe₂/Py/MgO/Ta were patterned into rectangular bars by photolithography and ion milling with the typical size of 20 × 60 μm². For conductivity and magnetotransport and magnetization switching, typical Hall-bar devices were made with 20 μm width by 35 μm length. After milling, the second step of photolithography and magnetron sputtering were employed to fabricate the Pt (5)/Au (70) electrical contact pads. Transport measurements were performed with a Keithley 2400 current source and a Keithley 2812 voltage meter in Quantum design PPMS system. In the ST-FMR measurements, the RF signals with frequencies from 3 to 12 GHz and a nominal max power of ≈14 dBm were applied along the longitudinal axis using a signal generator. The in-plane external magnetic field (*H*) was swept with an angle (ϕ) toward \hat{x} axis. Because the highest signal/noise ratio was obtained at 3–4 GHz, 4 GHz was usually chosen for angular dependent $V_{\text{mix}}(H, \phi)$ scanning, which was important for recording the weak signals in the thinnest stacks, e.g. PtTe₂ (5)/Py (2.5).

Supporting Information

Supporting Information is available from the Wiley Online Library or from the author.

Acknowledgements

This work was supported by the financial support from the National Key Research and Development Program of China [Grant Nos. 2016YFA0300802 and 2017YFA0206200], the National Natural Science Foundation of China [NSFC, Grant Nos.11874409, 11674373, 51801087, and 11804380], the Beijing Natural Science Foundation (Grant No. Z190009), the Strategic Priority Research Program (B) [Grant No. XDB07030200], the Key Research Program of Frontier Sciences (Grant No. QYZD1-SSW-SLH016), the International Partnership Program (Grant No. 112111KYSB20170090) of the Chinese Academy of Sciences (CAS), and the Fujian Innovation Academy, Chinese Academy of Sciences (Grant No. FJCY18040302). H.J. acknowledges the China Postdoctoral Science Foundation (No. 2019M650878). J.F. acknowledges the Youth Innovation Promotion Association of Chinese Academy of Sciences (Grant No. 2017010).

Conflict of Interest

The authors declare no conflict of interest.

Keywords

platina ditelluride, spin Hall conductivity, spin-orbit torque, thin film, type-II Dirac semimetal

Received: January 21, 2020

Revised: March 2, 2020

Published online:

- [1] A. Manchon, J. Zelezny, I. M. Miron, T. Jungwirth, J. Sinova, A. Thiaville, K. Garello, P. Gambardella, *Rev. Mod. Phys.* **2019**, *91*, 035004.
- [2] I. Mihai Miron, G. Gaudin, S. Auffret, B. Rodmacq, A. Schuhl, S. Pizzini, J. Vogel, P. Gambardella, *Nat. Mater.* **2010**, *9*, 230.
- [3] L. Q. Liu, C. F. Pai, Y. Li, H. W. Tseng, D. C. Ralph, R. A. Buhrman, *Science* **2012**, *336*, 555.
- [4] G. Q. Yu, P. Upadhyaya, Y. B. Fan, J. G. Alzate, W. J. Jiang, K. L. Wong, S. Takei, S. A. Bender, L. T. Chang, Y. Jiang, M. R. Lang, J. S. Tang, Y. Wang, Y. Tserkovnyak, P. K. Amiri, K. L. Wang, *Nat. Nanotechnol.* **2014**, *9*, 548.
- [5] M. Cubukcu, O. Boule, N. Mikuszeit, C. Hamelin, T. Bracher, N. Lamard, M. C. Cyrille, L. Buda-Prejbeanu, K. Garello, I. M. Miron, O. Klein, G. de Loubens, V. V. Naletov, J. Langer, B. Ocker, P. Gambardella, G. Gaudin, *IEEE Trans. Magn.* **2018**, *54*, 1.
- [6] C. F. Pai, Y. X. Ou, L. H. Vilela-Leao, D. C. Ralph, R. A. Buhrman, *Phys. Rev. B* **2015**, *92*, 064426.
- [7] X. P. Qiu, W. Legrand, P. He, Y. Wu, J. W. Yu, R. Ramaswamy, A. Manchon, H. Yang, *Phys. Rev. Lett.* **2016**, *117*, 217206.
- [8] W. F. Zhang, W. Han, X. Jiang, S. H. Yang, S. S. P. Parkin, *Nat. Phys.* **2015**, *11*, 496.
- [9] K. U. Demasius, T. Phung, W. F. Zhang, B. P. Hughes, S. H. Yang, A. Kellock, W. Han, A. Pushp, S. S. P. Parkin, *Nat. Commun.* **2016**, *7*, 10644.
- [10] L. J. Zhu, K. Sobotkiewich, X. Ma, X. Q. Li, D. C. Ralph, R. A. Buhrman, *Adv. Funct. Mater.* **2019**, *29*, 1805822.
- [11] L. Zhu, L. Zhu, M. Sui, D. C. Ralph, R. A. Buhrman, *Sci. Adv.* **2019**, *5*, eaav8025.
- [12] E. Derunova, Y. Sun, C. Felser, S. S. P. Parkin, B. Yan, M. N. Ali, *Sci. Adv.* **2019**, *5*, eaav8575.
- [13] N. H. D. Khang, Y. Ueda, P. N. Hai, *Nat. Mater.* **2018**, *17*, 808.
- [14] D. C. Mahendra, R. Grassi, J. Y. Chen, M. Jamali, D. R. Hickey, D. L. Zhang, Z. Y. Zhao, H. S. Li, P. Quarterman, Y. Lv, M. Li, A. Manchon, K. A. Mkhoyan, T. Low, J. P. Wang, *Nat. Mater.* **2018**, *17*, 800.
- [15] H. T. Yuan, M. S. Bahramy, K. Morimoto, S. F. Wu, K. Nomura, B. J. Yang, H. Shimotani, R. Suzuki, M. Toh, C. Kloc, X. D. Xu, R. Arita, N. Nagaosa, Y. Iwasa, *Nat. Phys.* **2013**, *9*, 563.
- [16] J. Sklenar, W. Zhang, M. B. Jungfleisch, W. J. Jiang, H. Saglam, J. E. Pearson, J. B. Ketterson, A. Hoffmann, *J. Appl. Phys.* **2016**, *120*, 180901.
- [17] K. Deng, G. L. Wan, P. Deng, K. N. Zhang, S. J. Ding, E. Y. Wang, M. Z. Yan, H. Q. Huang, H. Y. Zhang, Z. L. Xu, J. Denlinger, A. Fedorov, H. T. Yang, W. H. Duan, H. Yao, Y. Wu, S. S. Fan, H. J. Zhang, X. Chen, S. Y. Zhou, *Nat. Phys.* **2016**, *12*, 1105.
- [18] L. Y. Yang, N. A. Sinitsyn, W. B. Chen, J. T. Yuan, J. Zhang, J. Lou, S. A. Crooker, *Nat. Phys.* **2015**, *11*, 830.
- [19] X. Xu, W. Yao, D. Xiao, T. F. Heinz, *Nat. Phys.* **2014**, *10*, 343.

- [20] D. MacNeill, G. M. Stiehl, M. H. D. Guimaraes, R. A. Buhrman, J. Park, D. C. Ralph, *Nat. Phys.* **2017**, *13*, 300.
- [21] W. M. Lv, Z. Y. Jia, B. C. Wang, Y. Lu, X. Luo, B. S. Zhang, Z. M. Zeng, Z. Y. Liu, *ACS Appl. Mater. Interfaces* **2018**, *10*, 2843.
- [22] S. Hao, J. Zeng, T. Xu, X. Cong, C. Wang, C. Wu, Y. Wang, X. Liu, T. Cao, G. Su, L. Jia, Z. Wu, Q. Lin, L. Zhang, S. Yan, M. Guo, Z. Wang, P. Tan, L. Sun, Z. Ni, S.-J. Liang, X. Cui, F. Miao, *Adv. Funct. Mater.* **2018**, *28*, 1803746.
- [23] H. Huang, S. Zhou, W. Duan, *Phys. Rev. B* **2016**, *94*, 121117.
- [24] M. Z. Yan, H. Q. Huang, K. N. Zhang, E. Y. Wang, W. Yao, K. Deng, G. L. Wan, H. Y. Zhang, M. Arita, H. T. Yang, Z. Sun, H. Yao, Y. Wu, S. S. Fan, W. H. Duan, S. Y. Zhou, *Nat. Commun.* **2017**, *8*, 257.
- [25] A. R. Mellnik, J. S. Lee, A. Richardella, J. L. Grab, P. J. Mintun, M. H. Fischer, A. Vaezi, A. Manchon, E. A. Kim, N. Samarth, D. C. Ralph, *Nature* **2014**, *511*, 449.
- [26] Y. Wang, P. Deorani, K. Banerjee, N. Koirala, M. Brahlek, S. Oh, H. Yang, *Phys. Rev. Lett.* **2015**, *114*, 257202.
- [27] O. J. Clark, M. J. Neat, K. Okawa, L. Bawden, I. Markovic, F. Mazzola, J. Feng, V. Sunko, J. M. Riley, W. Meevasana, J. Fujii, I. Vobornik, T. K. Kim, M. Hoesch, T. Sasagawa, P. Wahl, M. S. Bahramy, P. D. C. King, *Phys. Rev. Lett.* **2018**, *120*, 156401.
- [28] K. Deng, M. Yan, C.-P. Yu, J. Li, X. Zhou, K. Zhang, Y. Zhao, K. Miyamoto, T. Okuda, W. Duan, Y. Wu, X. Zhong, S. Zhou, *Sci. Bull.* **2019**, *64*, 1044.
- [29] Y. L. Wang, L. F. Li, W. Yao, S. R. Song, J. T. Sun, J. B. Pan, X. Ren, C. Li, E. Okunishi, Y. Q. Wang, E. Y. Wang, Y. Shao, Y. Y. Zhang, H. T. Yang, E. F. Schwier, H. Iwasawa, K. Shimada, M. Taniguchi, Z. H. Cheng, S. Y. Zhou, S. X. Du, S. J. Pennycook, S. T. Pantelides, H. J. Gao, *Nano Lett.* **2015**, *15*, 4013.
- [30] C. Yim, K. Lee, N. McEvoy, M. O'Brien, S. Riazimehr, N. C. Berner, C. P. Cullen, J. Kotakoski, J. C. Meyer, M. C. Lemme, G. S. Duesberg, *ACS Nano* **2016**, *10*, 9550.
- [31] H. Xu, H.-P. Huang, H. Fei, J. Feng, H.-R. Fuh, J. Cho, M. Choi, Y. Chen, L. Zhang, D. Chen, D. Zhang, C. Ó. Coileáin, X. Han, C.-R. Chang, H.-C. Wu, *ACS Appl. Mater. Interfaces* **2019**, *11*, 8202.
- [32] Y. Zhou, H. J. Jang, J. M. Woods, Y. J. Xie, P. Kumaravadivel, G. A. Pan, J. B. Liu, Y. H. Liu, D. G. Cahill, J. J. Cha, *Adv. Funct. Mater.* **2017**, *27*, 1605928.
- [33] S. Dey, V. K. Jain, *Platinum Met. Rev.* **2004**, *48*, 16.
- [34] L. Fu, D. Hu, R. G. Mendes, M. H. Rummeli, Q. Dai, B. Wu, L. Fu, Y. Liu, *ACS Nano* **2018**, *12*, 9405.
- [35] H. Ma, P. Chen, B. Li, J. Li, R. Ai, Z. Zhang, G. Sun, K. Yao, Z. Lin, B. Zhao, R. Wu, X. Tang, X. Duan, X. Duan, *Nano Lett.* **2018**, *18*, 3523.
- [36] Z. Li, Y. Zeng, J. Zhang, M. Zhou, W. Wu, *Phys. Rev. B* **2018**, *98*, 165441.
- [37] L. Cheng, L. M. Wei, H. X. Liang, Y. D. Yan, G. H. Cheng, M. Lv, T. Lin, T. T. Kang, G. L. Yu, J. H. Chu, Z. Y. Zhang, C. G. Zeng, *Nano Lett.* **2017**, *17*, 6534.
- [38] S. Hikami, A. I. Larkin, Y. Nagaoka, *Prog. Theor. Phys.* **1980**, *63*, 707.
- [39] J. Mangin, P. Veber, *J. Cryst. Growth* **2008**, *310*, 3077.
- [40] L. Q. Liu, T. Moriyama, D. C. Ralph, R. A. Buhrman, *Phys. Rev. Lett.* **2011**, *106*, 036601.
- [41] Y. Wang, R. Ramaswamy, H. Yang, *J. Phys. D: Appl. Phys.* **2018**, *51*, 273002.
- [42] M. B. Jungfleisch, W. Zhang, J. Sklenar, J. Ding, W. Jiang, H. Chang, F. Y. Fradin, J. E. Pearson, J. B. Ketterson, V. Novosad, M. Wu, A. Hoffmann, *Phys. Rev. Lett.* **2016**, *116*, 057601.
- [43] K. Kondou, H. Sukegawa, S. Kasai, S. Mitani, Y. Niimi, Y. Otani, *Appl. Phys. Express* **2016**, *9*, 023002.
- [44] A. Kumar, S. Akansel, H. Stopfel, M. Fazlali, J. Akerman, R. Brucas, P. Svedlindh, *Phys. Rev. B* **2017**, *95*, 064406.
- [45] A. Ganguly, K. Kondou, H. Sukegawa, S. Mitani, S. Kasai, Y. Niimi, Y. Otani, A. Barman, *Appl. Phys. Lett.* **2014**, *104*, 072405.
- [46] H. An, T. Ohno, Y. Kanno, Y. Kageyama, Y. Monnai, H. Maki, J. Shi, K. Ando, *Sci. Adv.* **2018**, *4*, eaar2250.
- [47] Q. M. Shao, G. Q. Yu, Y. W. Lan, Y. M. Shi, M. Y. Li, C. Zheng, X. D. Zhu, L. J. Li, P. K. Amiri, K. L. Wang, *Nano Lett.* **2016**, *16*, 7514.
- [48] Y. Wang, D. P. Zhu, Y. Wu, Y. M. Yang, J. W. Yu, R. Ramaswamy, R. Mishra, S. Y. Shi, M. Elyasi, K. L. Teo, Y. H. Wu, H. Yang, *Nat. Commun.* **2017**, *8*, 1364.
- [49] J. H. Han, A. Richardella, S. A. Siddiqui, J. Finley, N. Samarth, L. Q. Liu, *Phys. Rev. Lett.* **2017**, *119*, 077702.
- [50] D. Wu, G. Yu, C.-T. Chen, S. A. Razavi, Q. Shao, X. Li, B. Zhao, K. L. Wong, C. He, Z. Zhang, P. K. Amiri, K. L. Wang, *Appl. Phys. Lett.* **2016**, *109*, 222401.
- [51] G. Q. Yu, P. Upadhyaya, K. L. Wong, W. J. Jiang, J. G. Alzate, J. S. Tang, P. K. Amiri, K. L. Wang, *Phys. Rev. B* **2014**, *89*, 104421.
- [52] M. Isasa, E. Villamor, L. E. Hueso, M. Gradhand, F. Casanova, *Phys. Rev. B* **2015**, *91*, 024402.
- [53] C. K. Safeer, J. Ingla-Aynés, F. Herling, J. H. Garcia, M. Vila, N. Ontoso, M. R. Calvo, S. Roche, L. E. Hueso, F. Casanova, *Nano Lett.* **2019**, *19*, 1074.
- [54] S. Y. Shi, S. H. Liang, Z. F. Zhu, K. M. Cai, S. D. Pollard, Y. Wang, J. Y. Wang, Q. S. Wang, P. He, J. W. Yu, G. Eda, G. C. Liang, H. Yang, *Nat. Nanotechnol.* **2019**, *14*, 945.
- [55] M. H. D. Guimaraes, G. M. Stiehl, D. MacNeill, N. D. Reynolds, D. C. Ralph, *Nano Lett.* **2018**, *18*, 1311.
- [56] G. M. Stiehl, R. Li, V. Gupta, I. E. Baggari, S. Jiang, H. Xie, L. F. Kourkoutis, K. F. Mak, J. Shan, R. A. Buhrman, D. C. Ralph, *Phys. Rev. B* **2019**, *100*, 184402.